# A Sparse-Mode Spectral Method for the Simulation of Turbulent Flows

M. Meneguzzi,* H. Politano,† A. Pouquet,† and M. Zolver†

*CERCA, 5160 Boulevard Décarie, Montréal, Québec H3X 2HP, Canada; on leave from CERFACS, Toulouse, France and †Observatoire de la Côte d'Azur, CNRS URA 1362, BP 229, 06304, Nice-cedex 4, France

We propose a new algorithm belonging to the family of the sparse-mode spectral method to simulate turbulent flows. In this method the number of Fourier modes **k** increases with $k$ more slowly than $k^{D-1}$ in dimension $D$, while retaining the advantage of the fast Fourier transform. Examples of applications of the algorithm are given for the one-dimensional Burgers' equation and two-dimensional incompressible MHD flows. © 1996 Academic Press, Inc.

## I. INTRODUCTION

In experimenting with turbulent flows using a computer, one is immediately faced with the enormous number of modes to be taken into account. Bounds on this number can be given on a basis akin to dimensional analysis of the Kolmogorov type [1], leading to a scaling in three dimensions,

$$M \sim R^{9/4}, \tag{1}$$

assuming that the energy spectrum (defined below) follows the Kolmogorov law $E(k) \sim k^{-5/3}$. Here, $M = N^3$ is the total number of modes in dimension three needed to yield a correct description of the flow down to the dissipative scale $\lambda_D = 2\pi/k_D$ with $k_D \sim R^{3/4}$, where $R = U_0 L_0/\nu$ is the Reynolds number, $U_0$ and $L_0$ being the characteristic velocity and scale of the flow, and $\nu$ is the kinematic viscosity. $N$ is the number of modes in each space direction. However, most of those modes are in the dissipative range. Indeed, let us define

$$E_k = \sum_{\mathbf{k} \in \mathscr{C}_k} E(\mathbf{k}) \tag{2a}$$

$$\mathscr{C}_k = \{\mathbf{k} | k \le |\mathbf{k}| < k + 1\} \tag{2b}$$

as the modal energy $E_k$ in spherical $k$-shells $\mathscr{C}_k$ of unit width constructed around the wavenumber $k + 1/2$ with $E(\mathbf{k}) = \frac{1}{2}\mathbf{v}_\mathbf{k}^2$ the energy of an individual velocity Fourier mode $\mathbf{v}_\mathbf{k}$. The number of modes in individual Fourier shells

$\mathscr{C}_k$ varies as $4\pi k^2$ in three dimensions; for a maximum wavenumber $k_{\max} = N/2$, and for a cutoff wavenumber at the end of the inertial range at $k_C = k_{\max}/C$, one finds that the ratio of the number of modes in the inertial range $N_I^3$ to the total number of modes $N^3$ scales like $C^{-3}$. For $C$ varying from 2 to 10 according to how well resolved the flow is, between 87% and 99.9% of the modes are in the dissipation range. For instance, for $N = 10^3$ in each direction, or an ensemble of $M = 10^9$ modes in three dimensions, of the one billion modes carried out numerically, only slightly more than one million belong to the inertial subrange. If, as is generally the case, one is interested mostly in this inertial subrange and in the early dissipation range, the simulation becomes very inefficient. Hence the spur to find appropriate models for these overwhelming noninertial modes.

One possibility is to resort to more or less sophisticated evaluations of transport coefficients, as for example in [2, 3]. However, the number of such coefficients grows with the growing complexity of the physical problem at hand, and so does the degree of arbitrariness in interscaling these coefficients.

In the same family of methods, although less physical *a priori* is the method to introduce numerical dissipation by resorting to a hyperviscosity algorithm whereby (a) the dissipative Laplacian operator written in Fourier space $k^2$ is replaced by $k^{2\alpha}$ with $\alpha > 0$; and (b) the coefficient in front of this hyperLaplacian can be either constant or field-dependent. These algorithms do ensure global positiveness of the dissipation; but such is not the case locally, giving rise to oscillations in the vicinity of sharp gradients. *Local* positivity of the hyperviscous operator can be enforced [4] but leads to a nonlinear viscosity which is more costly than the linear case to compute and more difficult to interpret since it can give rise to a *power-law* (as opposed to exponentially decreasing) early dissipation range. A comparison of these algorithms in the case of two-dimensional MHD has been performed in [5]; large-scale features of the flow are well reproduced and, more surprisingly, the location of small-scale dissipative layers as well. The latter

can be understood when one realises that such layers are at the border of large-scale eddies which are treated accurately.

Of a different nature are the sparse-mode algorithms. Various sparse-mode schemes have been proposed [6–8] in which only a subset of the *a priori* relevant Fourier modes is kept. The idea is that with a properly chosen subset, one can hope to have enough interactions among triads of wavevectors to retain all the nonlinear effects and to qualitatively model turbulent flows at a much lower cost. Such schemes rely on the fact that the conservation properties of quadratic invariants of the equations of motion also hold for truncated systems, in fact down to the basic triad interactions (for the quadratically nonlinear case) between three wavenumbers $(k, p, q)$ such that $\mathbf{k} = \mathbf{p} + \mathbf{q}$. These algorithms thus differ in how they reduce the set of wavenumbers and, also, in how drastic a reduction they propose. The Lorenz model [9] is an extreme case, with only three modes retained to describe the lack of predictability of convective atmospheric flows. Widely used, for example to study intermittency, are the shell-models first proposed in [6], in which only one mode per octave of wavenumber is kept.

However, when going from a full regular grid to an irregular set of wavenumbers, one loses the benefit of the fast Fourier transform (FFT), and evaluation of the nonlinear terms of the equations has to be done by explicit computation of convolution products. If the space dimension is $D$, and with $N$ modes in each direction, a convolution product takes $N^{2D}$ operations, while the spectral method using FFTs takes only $DN^D \log_2 N$ operations. The gain due to the FFT method is therefore $N^D/D \log_2 N$. For a sparse method to be able to compete with a full spectral method, the number of retained modes must thus be very small to compensate for this huge factor, and henceforth the representation of nonlinear interactions may become too crude.

The algorithm presented here is based on the same principles as the other sparse-mode methods but manages to retain the advantage of the FFT. The method is described in the next section. Its application to the Burgers' equation is dealt with in Section III, and the case of two-dimensional MHD is treated in Section IV. Section V is the conclusion.

## II. THE METHOD

The algorithm is explained for the case of one space dimension, but its extension to several dimensions is straightforward. Consider a periodic function $a(x)$ of period $2\pi$ defined on a grid of size $N$, where $N$ is a power of 2. In usual Fourier spectral methods (see, for instance, [10]) the function is represented by its $N$ Fourier components $a_k$, where $k$ is an integer going from $k_{\min} = -N/2 + 1$ to $k_{\max} = N/2$. As in all sparse mode methods, $a_k$ here is

allowed to be nonzero only for a subset of the Fourier modes.

We propose here that for $|k| \leq n/2$ all modes are retained, for $n/2 < |k| \leq n$ only even modes are retained, for $n < |k| \leq 2n$ only multiples of 4 are retained, and so on. This subset can be represented by $N_g$ embedded grids, with $2^{N_g-1} = N/n$; the grids are numbered from 0 to $N_g - 1$, such that grid 0 includes the modes with $|k| \leq n/2$, grid 1 includes only even modes with $|k| \leq n$, grid 2 multiples of 4 with $|k| < 2n$, etc. Let us call $G_j$ the subset of modes belonging to grid $j$.

Now suppose we want to compute the convolution product of two functions $a$ and $b$; $c_k = \sum_{l+m=k} a_l b_m$. This sum can be decomposed in the following way:

$$
\begin{aligned}
c_k = \sum_{l+m=k} a_l b_m &= \sum_{l+m=k, l, m \in G_0 \cup G_1} a_l b_m \\
&+ \sum_{l+m=k, l, m \in G_1 \cup G_2} a_l b_m + \cdots \\
&+ \sum_{l+m=k, l, m \in G_{N_g-2} \cup G_{N_g-1}} a_l b_m - \sum_{l+m=k, l, m \in G_1} a_l b_m \\
&- \cdots - \sum_{l+m=k, l, m \in G_{N_g-2}} a_l b_m.
\end{aligned}
\tag{3}
$$

What makes this decomposition possible is that the modes of grid $j$ have nonlinear interactions only with modes of grids $j - 1$ and $j + 1$. The sums preceded by a $-$ sign compensate for double counting of interactions among modes common to two grids. Each term of this decomposition can be computed independently using a grid of size $2n$ for the terms preceded by a $+$ sign, and a size $n$ for the others. Therefore, one FFT of size $N$ is replaced by several FFTs of size $2n$ or $n$. For a number of grids $N_g$ larger than 2, there is a net economy in computation. For instance, in dimension three, for $N = 1024$ and $n = 128$, one finds that the sparse method is 25 times faster than the full spectral method. Memory requirements are also much lower (a $1024^3$ simulation is barely feasible on present-day computers).

All these partial sums must of course be dealiased for the above decomposition to be meaningful. This can be done by the usual method of taking a larger grid (by a factor 3/2 for quadratic nonlinearities) to compute the FFTs.

In the grid in which all Fourier modes are retained, this does *not* mean that for these modes the nonlinear interactions are entirely correct, since some of them—in particular close to the first cutoff $k_{\max}^{(1)}$—are missing, namely those corresponding to couplings with the deleted modes. However, in many applications, it is well known that nonlinear transfer is mostly local in wavenumber; i.e., it is dominated by triad interactions within which the ratio
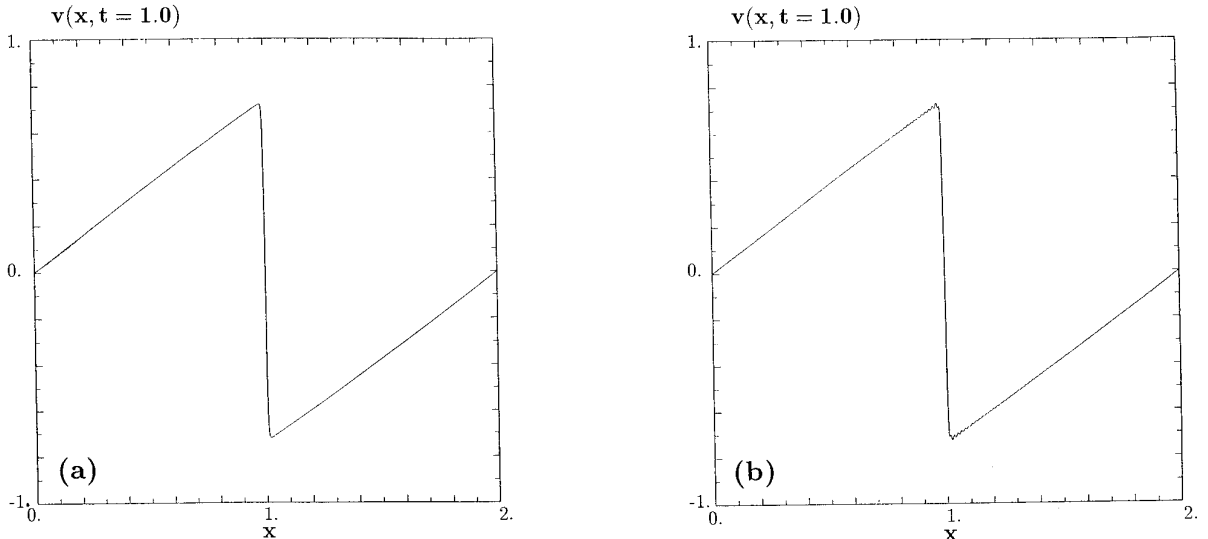
v(x, t = 1.0)                                          v(x, t = 1.0)



**FIG 1.** Velocity profile for the Burgers' equation at $t = 1$ for (a) the test run and (b) the sparse-mode run. Simulations with $k_{max} = 1024\pi$, and $\nu = 0.002$.

of the largest to the smallest wavenumber is at most $\sim 4$ (see [11] for a recent analysis and review). The choice of the wavenumber $k_{max}^{(1)}$ at which the first reduced grid is begun depends on how far down in wavenumber one wants to retain all modes, i.e., on the problem at hand. In the MHD case described in Section IV, two choices of $k_{max}^{(1)}$ are compared.

## III. APPLICATION TO THE BURGERS' EQUATION

The sparse-mode method just described is now applied to a one-dimensional case, the Burgers' equation,

$$\frac{\partial v}{\partial t} = \frac{\partial}{\partial x}\frac{v^2}{2} + \nu\frac{\partial^2 v}{\partial x^2}, \qquad (4)$$

where $\nu$ is the viscosity. We take for initial condition $v(x, 0) = -\sin(\pi x)$ for $-1 \le x \le +1$ and $\nu = 0.002$, with $k_{max} = 1024\pi$; the solution develops a shock at $t = 1/\pi$. The equation is integrated first by a standard Fourier spectral method using a grid $N = 2048$ (test run); the same calculation is done using the sparse-mode method described above with $n = 256$ and therefore $N_g = 4$ grids (sparse run); here, a conservative choice is made and the wavenumber, until which all modes are kept ($k_{max}^{(1)} = 128\pi \sim 400$), is already in the dissipation regime with this choice of viscosity.

Figures 1 show the velocity at time $t = 1$, for the test run (a) and the sparse run (b), and Figs. 2 show in lin–log coordinates the energy spectrum of the solution $E(k, t) = \frac{1}{2}|v_k(t)|^2$ at the same time, for the test run (a) and the sparse run (b). Similarly, the energy spectra in log–log coordinates

are displayed in Figs. 3. From Figs. 1, one can see the good agreement between the two computed values of the velocity field $v(x, t)$. Note, however, the small oscillations near the shock, due to a Gibbs phenomenon generated by the "holes" in Fourier space, where $v_k = 0$. Also, it is clear from Figs. 2 that the spectra are almost identical for $k < k_{max}^{(1)}(=128\pi)$, that is, for $k$ belonging to grid 0. At $k \sim 400$ one detects a cusp in the sparse-mode spectrum due to the absence of odd modes for $k > k_{max}^{(1)}$. A second cusp at $k = 2k_{max}^{(1)}$ is barely visible. Beyond $k = k_{max}^{(1)}$, there is a discrepancy in the two spectra. The exponential tail of the spectrum due to viscous effects decreases faster in the sparse-mode result than in the test run (Figs. 3). However, the difference remains small and does not affect the low-wavenumber part of the spectrum, which follows the expected power law $E_k \sim k^{-2}$ up to $k \sim 100$.

In the inertial domain, the two spectra are identical within three digits. This test is particularly severe because in one dimension there is no smoothing effect due to angle average, when computing an energy spectrum.

## IV. TWO-DIMENSIONAL MHD FLOWS

### IV. 1. *Equations*

When more than one field variable is involved, does the proposed algorithm reproduce correctly the interactions between such fields? One may think of the coupling to a temperature field (passive scalar), or the compressible case. Here we wish to address this problem in the context of a conducting fluid following the MHD equations for the velocity and the magnetic field. In this case, it is known
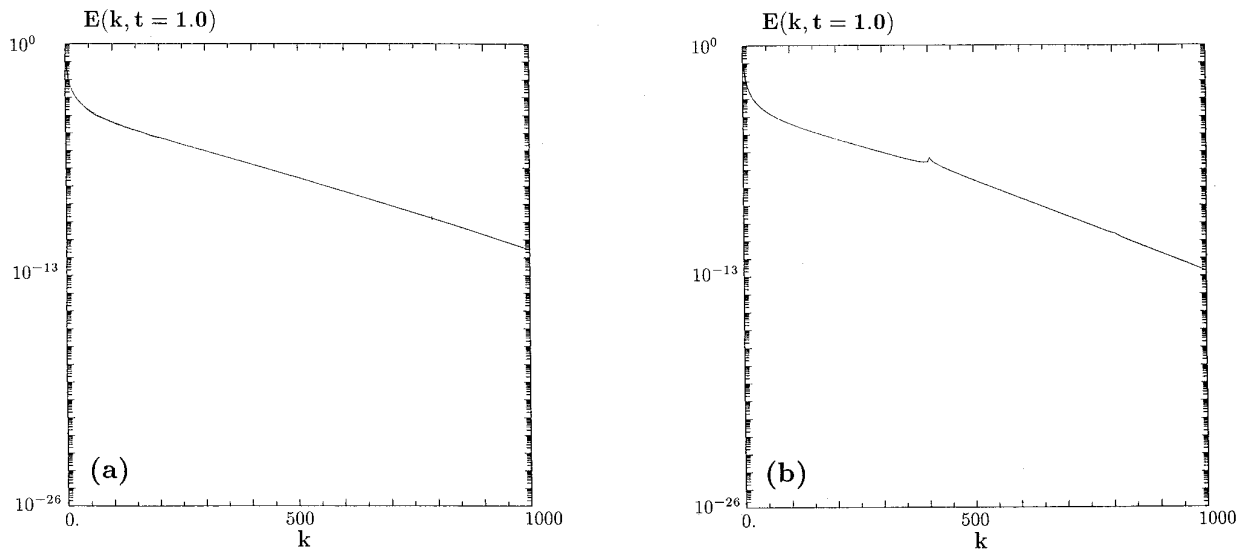
**FIG. 2.** Energy spectra at $t = 1$ in lin–log coordinates for (a) the test run and (b) the sparse-mode run for the same simulations as in Fig. 1.

that the nonlinear interactions are partly nonlocal; a large-scale quasi-uniform magnetic field gives rise to Alfvén waves that propagate transversely along the field lines. This in turn diminishes the efficiency of the nonlinear interactions, and the resultant energy spectrum $E^T(k)$ defined below, in the absence of significant correlations between the velocity and magnetic field, is shallower than in the Navier–Stokes case [12, 13], namely $E^T(k) \sim k^{-3/2}$.

The MHD equations are now given in the incompressible limit for the velocity field $\mathbf{v}$ and for the Alfvén velocity $\mathbf{b} = \mathbf{B}/\sqrt{\mu\rho_0}$, where $\mathbf{B}$ is the induction, $\mu$ is the permeability in empty space, and $\rho_0$ is the uniform density; in a form that brings out the similarity with the Navier–Stokes equations, they read

$$\frac{\partial \mathbf{v}}{\partial t} + \mathbf{v} \cdot \nabla \mathbf{v} = -\nabla \left( P + \frac{b^2}{2} \right) + \nu \nabla^2 \mathbf{v} + \mathbf{b} \cdot \nabla \mathbf{b}, \quad (5a)$$

$$\frac{\partial \mathbf{b}}{\partial t} + \mathbf{v} \cdot \nabla \mathbf{b} = \mathbf{b} \cdot \nabla \mathbf{v} + \eta \nabla^2 \mathbf{b}, \quad (5b)$$
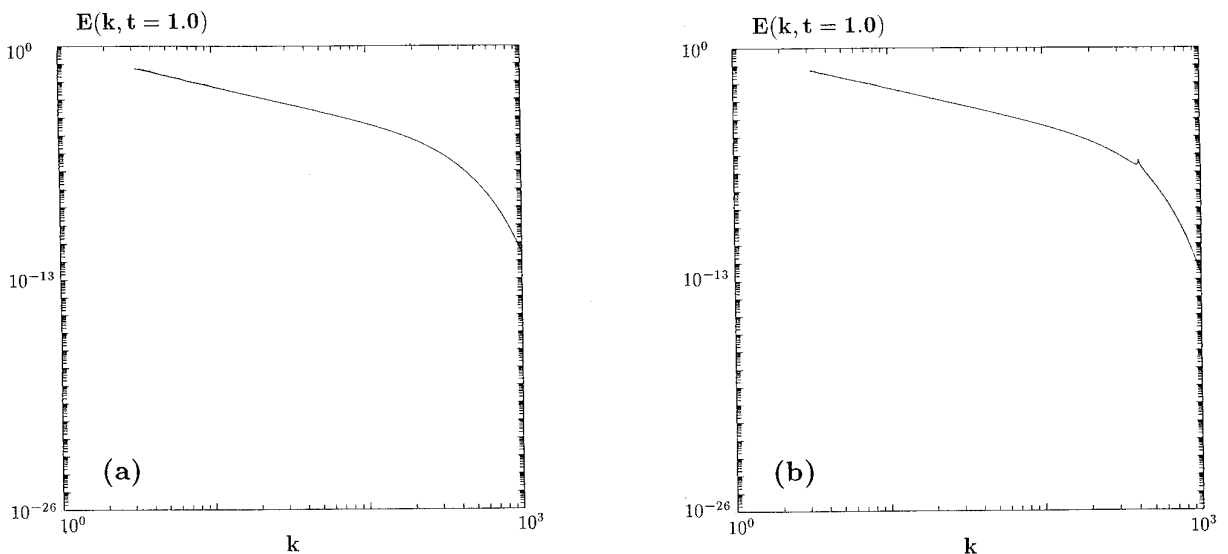


**FIG. 3.** Energy spectra at $t = 1$ in log–log coordinates for (a) the test run and (b) the sparse-mode run for the same simulations as in Figs. 1 and 2.

$$\nabla \cdot \mathbf{v} = 0, \tag{5c}$$

$$\nabla \cdot \mathbf{b} = 0, \tag{5d}$$

with the current density being defined as $\mathbf{j} = \nabla \times \mathbf{b}$; $\nu$ is the kinematic viscosity and $\eta$ is the magnetic diffusivity; they will be taken equally in what follows (unit magnetic Prandtl number); $P$ is the pressure.

We shall now test the sparse-mode method on two-dimensional MHD. A prototype of MHD flows in two dimensions is the commonly studied Orszag–Tang vortex [14] which takes as initial conditions expressed in terms of the stream function $\psi$ with $\mathbf{v} = \nabla \times \psi$ and, equivalently, the magnetic potential $A$ with $\mathbf{b} = \nabla \times A$:

$$\psi_0 = 2(\cos x + \cos y),$$

$$A_0 = 2 \cos x + \cos 2y;$$

it corresponds to a magnetic neutral $X$-point embedded in a large-scale eddy and centered on the stagnation point of the velocity. It yields to the development of several current sheets, the strongest one being at the center of the computational box [15–17] of length $L_0 = 2\pi$. This flow, and variants in which the velocity-magnetic field correlation coefficient is lower, has also been studied in the context of modeling small-scale flows with either a high power of the Laplacian operator [5, 18] or with field-dependent nonlinear transport coefficients [5]. In the former case, the dissipation is not positive everywhere in space, leading to oscillations near quasi-discontinuities. In the latter, the extra nonlinear terms introduced by the modelisation of small scales are costly, because they involve the computation of extra FFTs. Moreover, nonlinear eddy viscosities may lead to a power-law dissipation range, which will interfere with the inertial range; the empirical adjustment of the pseudo-viscosity coefficients is also more delicate.

Here we shall compare the results of seven runs, as listed in Table I; $N_g$ is the number of grids used (test runs are with $N_g = 1$), and $k_{\max}^{(1)}$ is the wavenumber beyond which the first modified grid begins (the maximum wavenumber of the computation when $N_g = 1$). Test runs M1 and M4 are not dealiased, whereas the test run M7 is computed up to $t = 1.4$ on a grid of $768^2$ points with the usual two-thirds dealiasing rule, yielding $k_{\max} = 256$ as for runs M4–M6.

In the computations to be described, the choice of $k_{\max}^{(1)}$ was guided by the following considerations. It is known [15–17] that in a well-resolved Orszag–Tang flow, the wavenumber at which one begins to feel dissipative effects at a viscosity $\nu = 0.001$ is at most $k_D \sim 40$. Note that, assuming a linear scaling with viscosity, this means that for runs M1–M3, we should have $k_D \sim 10$, whereas for runs M4–M7, $k_D \sim 20$. This conclusion was reached

### TABLE I

MHD Runs Described in This Paper, Together with the Viscosity $\nu$ (with $\nu = \eta$), the Number of Grids Used $N_g$ ($N_g = 1$ Corresponding to Test Cases), and the Maximum Wavenumber $k_{\max}^{(1)}$ for Which the Full Span of Wavenumbers Are Employed

| Run | $\nu$ | $N_g$ | $k_{\max}^{(1)}$ | Note |
|---|---|---|---|---|
| 13—M1 | 0.0050 | 1 | 128 | Fully aliased |
| 1—M2 | 0.0050 | 3 | 32 | |
| 2—M3 | 0.0050 | 4 | 16 | |
| 14—M4 | 0.0025 | 1 | 256 | Fully aliased |
| 4—M5 | 0.0025 | 3 | 64 | |
| 3—M6 | 0.0025 | 4 | 32 | |
| 5—M7 | 0.0025 | 1 | 256 | |

*Note.* The runs M1 and M4 are fully aliased; all other runs are dealised.

through two types of criteria. On the one hand, using a best fit to the computed energy spectra in the form $E(k, t) \sim C(t)k^{-m(t)}e^{-\beta(t)k}$, the inverse of the logarithmic decrement $\beta$ gives a first estimate. On the other hand, one can measure the width of the computed energy flux while it remains constant with wavenumber, a sign of quasi-inviscid nonlinear transfer to small scales; the flux is defined as $\Pi(k) = \int_0^k T(p) \, dp$, where $T(k) = \hat{v}(k)\partial_t^{(0)}\hat{v}(k) + \hat{b}(k)\partial_t^{(0)}\hat{b}(k)$ is the nonlinear transfer of the total energy

$$E^T = E^V + E^M = \tfrac{1}{2}\int (\mathbf{v}^2 + \mathbf{b}^2)d^2\mathbf{x} = \int E^T(k) \, dk$$

of Fourier spectrum $E^T(k)$. Note that the time derivatives are meant to be taken *in the nondissipative case,* with $\partial_t^{(0)}$ meaning that both $\nu$ and $\eta$ have been set $\equiv 0$ in Eqs. (5).

We thus took two possible values for $k_{\max}^{(1)}$ in the vicinity of $k_D$ according to the above estimates, a choice less conservative than the one made for the Burgers' equation (see Section III).

### IV. 2. *Statistical Variables*

In Figs. 4, we show the temporal variation of the total enstrophy (left)

$$\Omega^T = \int k^2 E^T(k) \, dk,$$

with $\mathscr{D}^T = 2\nu\Omega^T$ the total dissipation in the flow (in the case of a unit magnetic Prandtl number, as assumed here) and of the total energy (right) for runs M1 (solid line) and M2 (dashed line). The total enstrophy is maximum at $t \sim 1.2$, around which time dissipation sets in because of the formation of small-scale structures in the form of vorticity quadrupoles [19] and current sheets. Whether the limit, for zero viscosity and magnetic diffusivity, of the dissipa-
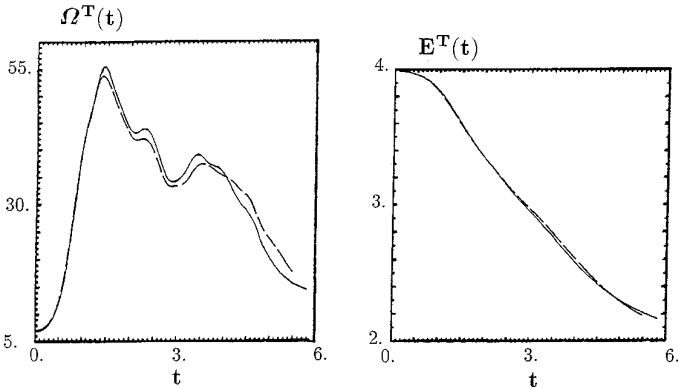
**FIG. 4.** Temporal variation of the total enstrophy (left) and the total energy (right) for two-dimensional MHD; test run M1 (solid line) and sparse run M2 (dashed line). The nomenclature of runs is given in Table I. Note the close similarities between the two runs.

tion $\mathscr{D}^T$ is finite or not is an open problem of great interest in astrophysics, in particular in the context of solar flares and the heating of the solar corona, a problem that requires huge numerical resolutions in view of the large Reynolds numbers to be considered [20] and for which the present algorithm may be useful.

All these global quantities are very similar for both runs, including the enstrophies which stress the small-scale dynamics, with in particular a secondary maxima around $t \sim 3.5$ linked to reconnection processes of magnetic field lines [15]. The time-scale of Alfvénic oscillations between kinetic and magnetic energy (not shown) is also well reproduced. Almost identical results obtain for run M3. A similar conclusion concerning averaged quantities can be drawn when comparing the higher resolution runs M4–M7.

However, a more detailed inspection of individual modal energies $E(k)$ as defined in Eqs. (2) alters somewhat this conclusion. Figures 5 display for run M6 (a, c) and the test run M4 (b, d) the temporal variation of $E(k = 20)$ (a, b) and $E(k = 40)$ (c, d) on either side of the first grid cutoff $k_{max}^{(1)} = 32$. Whereas in the former case, little alteration due to the proximity of the onset of the first decimation grid is visible, the effect of the decimation is strongly felt in the latter, both in the overall temporal variation and in the actual amplitudes of the modal energy. This is not surprising, since for an equivalent dissipation of energy, this dissipation occurs through a substantially smaller number of modes which individually must be more efficient in removing the energy coming from the inertial range at a rate $\varepsilon$ fixed by the initial conditions.

Let us define the discrepancy factor:

$$\Delta_1 = E(k_{max}^{(1)})/E(k_{max}^{(1)} + 1).$$

With definition (2) of the shells unchanged for the $N_g =$

1 and the $N_g \neq 1$ runs, we should have $\Delta_1 \sim 4$, corresponding to the average ratio of the number of points in the shell centered on $k_{max}^{(1)}$ and in the shell next to it, an effect superimposed to the local (intrinsic) variation of the energy spectrum. For example, in run M6, this discrepancy is largest at $t \sim 1.15$ (with $\Delta_1 \sim 4.06$) and lowest at $t \sim 3.4$ (with $\Delta_1 \sim 1.73$), with an average value around $\sim 3$. The fact that this average value is less than 4 shows that there is backscattering, a phenomenon which is linked to the issue of loss of predictability in turbulent flows, since the small scales can act as an eddy-force for the large scales through a beating mechanism. Let $m_a(k)$ be the actual number of points in a given Fourier shell $k$, $m_t(k)$ the theoretical number of points in this shell (in two dimensions, $m_t(k) = 2\pi k$) and $r(k)$ their ratio; it is clear that $r(k_{max}^{(1)})/r(k_{max}^{(1)} + 1) \sim 4$, hence the problems visible on the spectra.

In Figs. 6 the energy spectra for runs M5 (a) and M7 (b) are displayed in log–log coordinates. The small gaps at high wavenumber for the spectrum (6a) are due to the fact that some of the unit-width shells defined in (2) are somewhat depleted. This effect is more strongly felt in run M6 (not shown) after the third cutoff ($k > k_{max}^{(3)} = 128$) for which only one mode in 64 is actually followed in time. We choose here to represent data in identical ways for multigrid runs and for test runs, so that this depletion is clearly seen. On the other hand, four adjacent shells might in fact be added in plotting spectra in the first reduced grid, 16 shells in the next grid, etc. to avoid such holes; a weighing algorithm taking into account the ratio of the actual to the theoretical number of points $2\pi k$ in a two-dimensional shell of mean radius $k$ and width $\Delta k = 1$ might also be used.

The correlation between the velocity and magnetic field is defined as

$$E^C(x, y) = \mathbf{v}(x, y) \cdot \mathbf{b}(x, y).$$

Integrated over the whole domain, $E^C$ is an invariant of the nondissipative ($\nu = 0$, $\eta = 0$) MHD equations. Its Fourier spectrum is $E^C(k)$. We define as well the correlation coefficient

$$\rho(x, y) = \mathbf{v}(x, y) \cdot \mathbf{b}(x, y)/(|\mathbf{v}(x, y)|^2 + |\mathbf{b}(x, y)|^2). \quad (6)$$

With this definition, it is bounded by $\pm 0.5$, as, for example, when the flow consists of a pure spectrum of Alfvén waves $\mathbf{v} = \pm\mathbf{b}$; in this case the nonlinear terms of the MHD equations are identically zero, as immediately seen in Eqs. (5). We plot in Figs. 7 at $t = 1.2$ the fourth-order moment of that spectrum, i.e., $k^4 E^C(k)$, in order to emphasize the effect of small scales, for runs M7 (a) and M6 (b). No serious discrepancy can be seen in such curves. However, the Fourier spectrum $\hat{\rho}(k)$ of the correlation coefficient
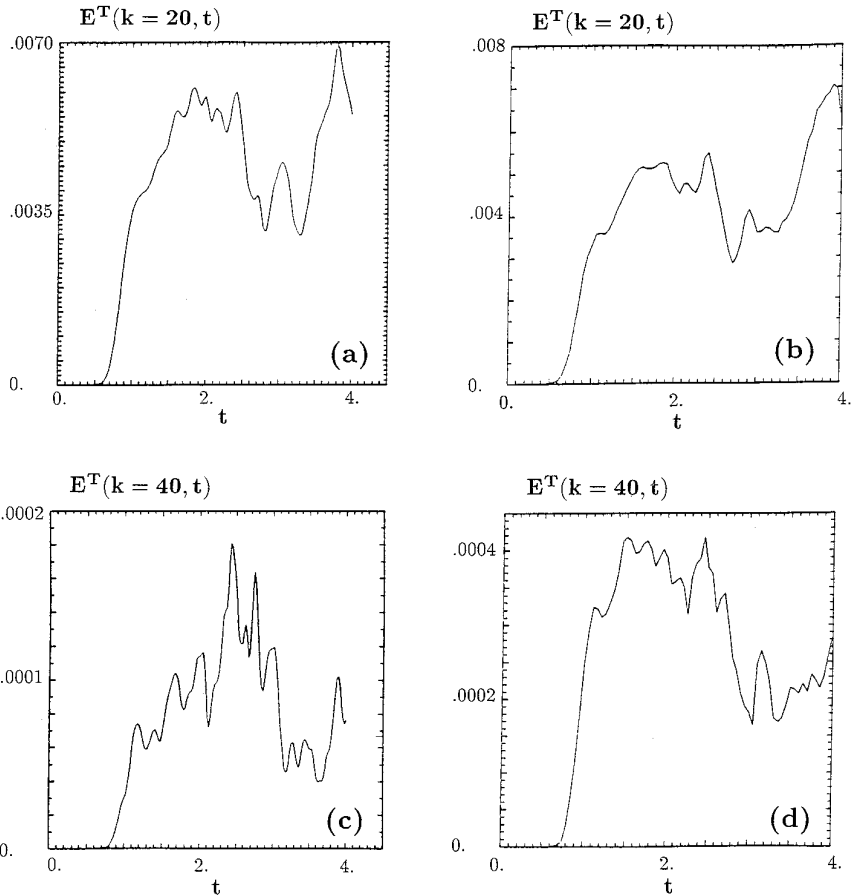
**FIG. 5.** Temporal variation of modal energies defined in (2) for (a, b) $k = 20$ and (c, d) $k = 40$ for the MHD runs M6 (a, c) for which $k^{(1)}_{\max} = 32$, and the test run M4 (b, d).
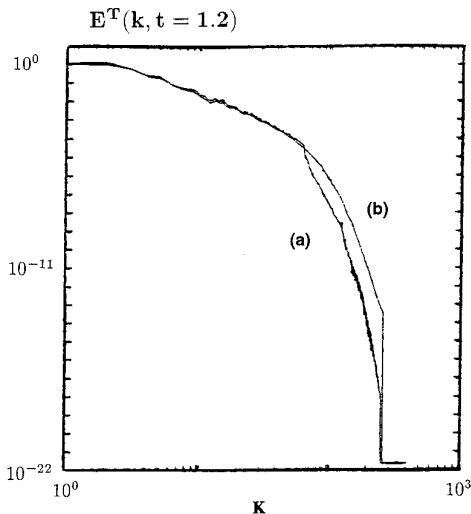
**FIG. 6.** Total energy spectra at $t = 1.2$ for the sparse run M5 (a) and the test run M7 (b). Some shells are depleted for the multigrid run (see text).

(Figs. 7c for the test run M7, and 7d for run M6) is very sensitive to the depletion in wavenumbers as we go from one grid to the next; the effect is particularly conspicuous at $k = k^{(1)}_{\max}$. We checked that this was not a systematic effect; the difference in the computed values of $\hat\rho(k)$ between the test run and the multigrid run varying wildly around zero from individual mode to individual mode within a given Fourier shell (not shown). In fact, in the fully aliased run M4 a similar error arises close to the cutoff wavenumber $k_{\max} = 256$. This simply shows that this variable is very sensitive to the velocity and magnetic fields being close to zero. We should also recall that it is expected both from analytical studies and closure models of turbulence (see, for example, [21]) that the spectrum of the correlation coefficient changes sign in the vicinity of the dissipative wavenumber $k_D$ [22], once the flow has reached the small scales. This would be a further argument to set $k^{(1)}_{\max} \sim k_D$.

In Figs. 8 probability distribution functions for the test run M7 (a, c) and the sparse run M6 (b, d) at $t = 1.4$ for the derivatives $\partial_y v_x$ (a, b) and $\partial_y b_x$ (c, d) of the velocity and the magnetic field are displayed. Values on the $x$-
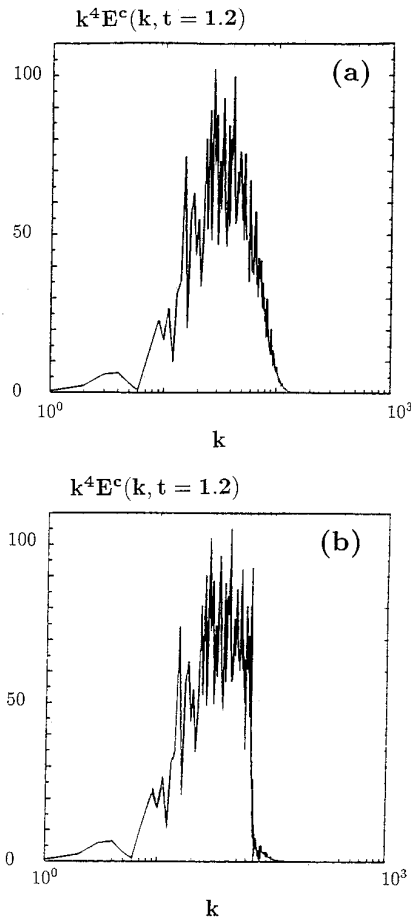
$k^4 E^c(k, t = 1.2)$

(a)



$k^4 E^c(k, t = 1.2)$

(b)

**FIG. 7.** Fourth moment of the correlation spectrum $k^4 E^C(k)$ (see text for definition) at $t = 1.2$ for the test run M7 (a) and the sparse run M5 (b).

axis are in arbitrary units. The dotted line represents the Gaussian distribution with the same dispersion. The fields themselves have, both for the test run and the sparse-mode scheme, quasi-Gaussian profiles (not shown). This type of diagnostic is useful to show the effect of the increased intermittency of small scales, with strong exponential departures in the wings of the distribution functions for the small-scale data. This is yet another test of the decimation algorithm which confirms its validity, in so far as it can reproduce accurately such departures from Gaussian profiles in the wings of the pdf of small-scale velocity and magnetic fields.

### IV. 3. *Contours of Field Variables*

We now turn our comparison to an inspection of contours in physical space. We again concentrate on the high resolution runs at a time close to the peak of the enstrophy. In Figs. 9 we show the magnetic potential $A$ for the test run M7 (a) and the sparse runs M5 (b) and M6 (c) at $t =$

1.2. Only the central window is displayed, centered on the point $(\pi, \pi)$. Whereas the stream functions for those three runs look almost identical (not shown), the magnetic potentials differ in an essential way locally; indeed a central island, more visible in run M6, emerges in the multigrid runs, corresponding to a cut of the contour line $-1.10$, more significant than in the test run. In run M6, the island is not drawn, since it has not reached the $-1.10$ level, but the high at a level of $-1.12$ is indicated. In all three cases, though, note that the minima are identical.

In Figs. 10 we show the full $\psi$ (a, b) and $A$ (c, d) fields at a later time ($t = 4.0$) for runs M4 (a, c) and M6 (b, d). Again the stream functions are quite similar, but the central magnetic island has grown to a sizable dimension in the M6 run. However, the similarities in the two flows in most of the box is at the origin of the good agreement found in Figs. 4 for global energetic quantities. Note also the presence of a central eddy in the stream functions for both the test run and the sparse run.

Figures 11 show the correlation coefficient defined in Eq. (6) in the central window at time $t = 1.2$ for runs M7 (a) and M6 (b). The sparse-mode run is noisy around the zero level, as already discussed in the context of Figs. 7. Whereas the correlation coefficient integrated over the whole computational box is equal to 0.26 for runs M6 and M7 at that time, we see from inspection of Figs. 11 that, in the multigrid run, as well as in the test run, this average (integrated) value is well below local values close to the extrema of $\rho$ at $\pm 0.5$. Again, the multigrid run reproduces that fact closely, of alternate regions in space where the velocity and magnetic fields are either parallel or anti-parallel as for Alfvén waves. As noted before, such configurations lead to a substantial reduction of the nonlinear dynamics of the MHD equations (5), a reduction that might not have been thought of from the simple inspection of the averaged global value of the correlation coefficient $\rho$. Different computations with random initial conditions led to the same conclusion; they also indicated that the regions of space where $\rho$ is within $\pm 10\%$ of its minimum value, are sparse [5]. Hence a soft (weak) MHD turbulence in two dimensions, a result that may or may not extend in dimension three and is one important open problem in 3D. Furthermore, as is well known, the correlation between the velocity and the magnetic field grows with time. At the maximum of the enstrophy ($t = 1.2$), the correlation coefficient has grown by 4.43% in the aliased test run M4 (and 4.42% in the dealiased one M7), whereas the growth is 4.41% in the run M5 with three grids and 4.19% in the run M6 with four grids. At $t = 4$, the growth is 26.7% in run M6 and 29.2% in run M4. This velocity-magnetic field correlation becomes more striking visually than at earlier times, as can be seen in Figs. 10.

In Figs. 12, we show the current density $j$ at $t = 1.2$ for runs M4 (a) and M6 (b). Contour intervals are every 10
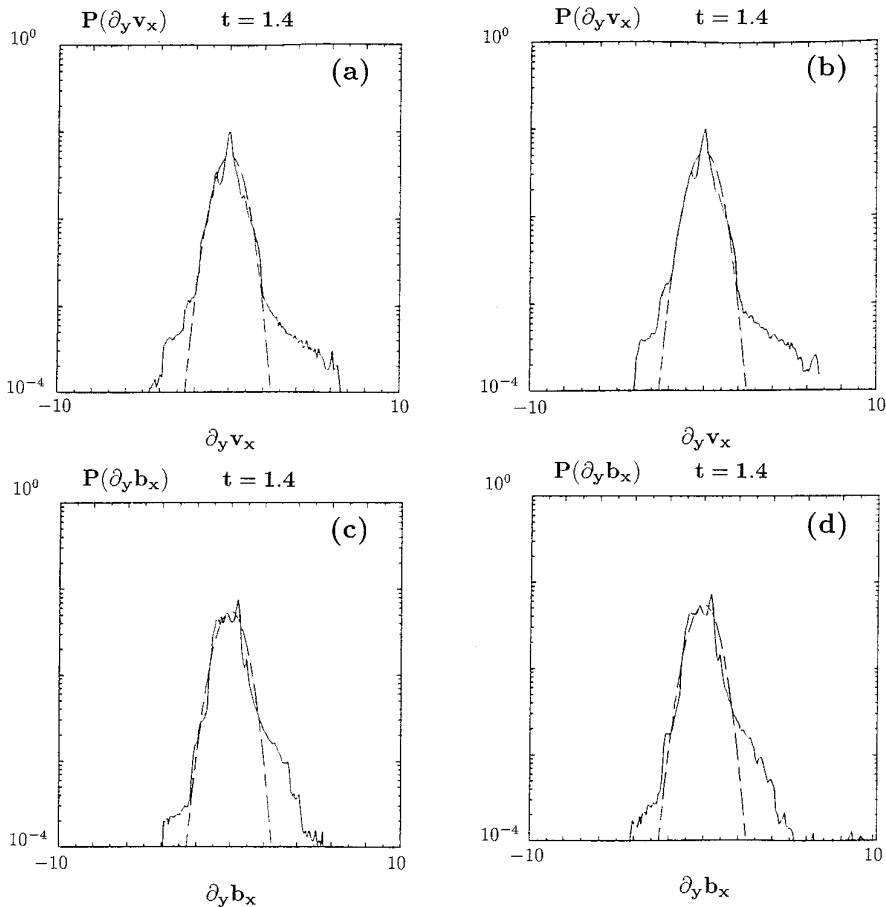
**FIG. 8.** Probability densities at $t = 1.4$ of the derivatives $\partial_y v_x$ (a, b) and $\partial_y b_x$ (c, d) of the velocity and the magnetic field for the MHD runs M7 (a, c) and M6 (b, d). The dotted line is a Gaussian fit to the data. Note the similar exponential wings for both runs.

for run M4 and twice that for run M6. All current filaments appear in the multigrid run, with decreased (by roughly 10%) central peaks. However, the decimation algorithm produces oscillations around the 0-level that are absent in the well-resolved test run, a phenomenon that tends to be emphasized by contour algorithms.

Finally, Figs. 13 show a scatter plot of the $xx$-component of the tensor $p_i p_j$, where $\mathbf{p} = \mathbf{v} + \mathbf{b}$; it can be viewed as a generalized Reynolds-stress tensor. The test run M7 is in abscissa ($x$), and the sparse-model run M6 is on the ordinate ($y$); (a) is the full data, and (b) is the data in which large scales have been filtered out; only wavenumbers larger or equal to the first grid cutoff $k_{max}^{(1)} = 32$ are retained. The lines drawn by least-square fit can be written as $y = fx + g$ with $f = 0.99997$ (resp. $f = 0.894$ for the filtered data), and $g = 5.0 \ 10^{-4}$ (resp. $g = 5.6 \times 10^{-4}$). This shows an excellent agreement between the total stress tensors. However, comparison of the high-pass-filtered stresses (which are represented by a subgrid model in LES) shows some discrepancy, as expected. The two data set becomes quasi-uncorrelated when the filtering is done above $k =$

63 (not shown). In the LES formulation, the data given here would represent part of the generalized Reynolds-stress for the filtered fields.

### IV. 4. *Assessment of the Method in MHD*

As a conclusion, we can state that in the two-dimensional MHD case, the multigrid algorithm behaves satisfactorily, both for global temporal variations and for contours of the velocity and magnetic fields, including small-scale features.

However, a closer inspection of data does reveal a detailed difference concerning the precise way in which the central current sheet destabilises under the tearing mode. It is well known that this instability, corresponding to the formation of magnetic islands better displayed in the magnetic potential, is very sensitive to several factors—for example, for different Reynolds numbers, or for identical physical parameters but different time steps, or with the addition of a small perturbation to the basic flow. All contribute to differing results, such as the number of islands appearing in the magnetic potential, or the time at which they appear (reconnection time). The aspect ratio of the
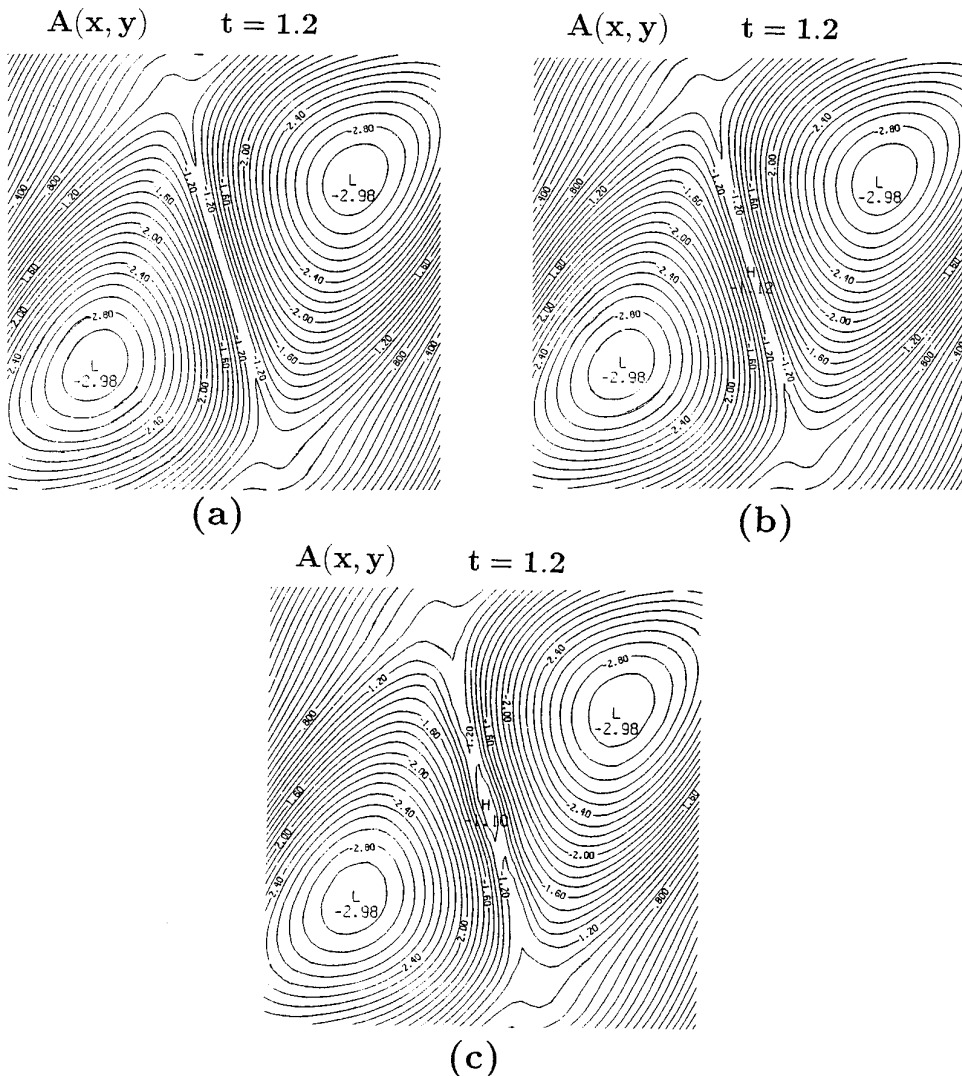
A(x, y)      t = 1.2

A(x, y)      t = 1.2

(a)

(b)

A(x, y)      t = 1.2

(c)

**FIG. 9.** Contour lines of the magnetic potential at $t = 1.2$ for the MHD runs M7 (a), M5 (b), and M6 (c). Only the window on the central current sheet is represented.

sheet plays a role as well, and it may again be affected by the multigrid algorithm. Furthermore, the noise introduced by the suppression of high-$k$ modes in the sparse-mode calculation is much higher than the usual truncation error of direct spectral simulations and can trigger tearing instabilities sooner. Such discrepancies in the small-scales and the fact that such scales are noisy is also found in other LES methods for MHD. It is therefore not surprising that the precise reconnection process occurs differently for multigrid runs. Although it may ultimately for much larger resolutions also alter the global aspect of flows, in particular, if secondary peaks in the enstrophy (such as the one at $t \sim 3.5$; see Figs. 4a, b) become dominant, such is not the case in the study presented here. This point would require substantially larger computing power to be settled.

Finally, we should mention the savings in computing power obtained when using the sparse-mode code in two-dimensional MHD. Multigrid runs M5 and M6 require respectively 4% and 10% of the memory needed by run M7, and 19% and 50% less CPU time than run M7. Larger gains should be expected in three dimensions. Moreover, for three-dimensional problems for which the actual available memory of computers is the direst need, the significant gain in memory (larger than the corresponding gain in CPU) of the algorithm is particularly attractive.

## V. CONCLUSION

We have developed a new algorithm which allows cutting computational costs of spectral simulations of turbulent flows, while retaining an accurate description of the nonlinear interactions in the inertial range. It makes use of a sparse Fourier mode representation of the fields in the
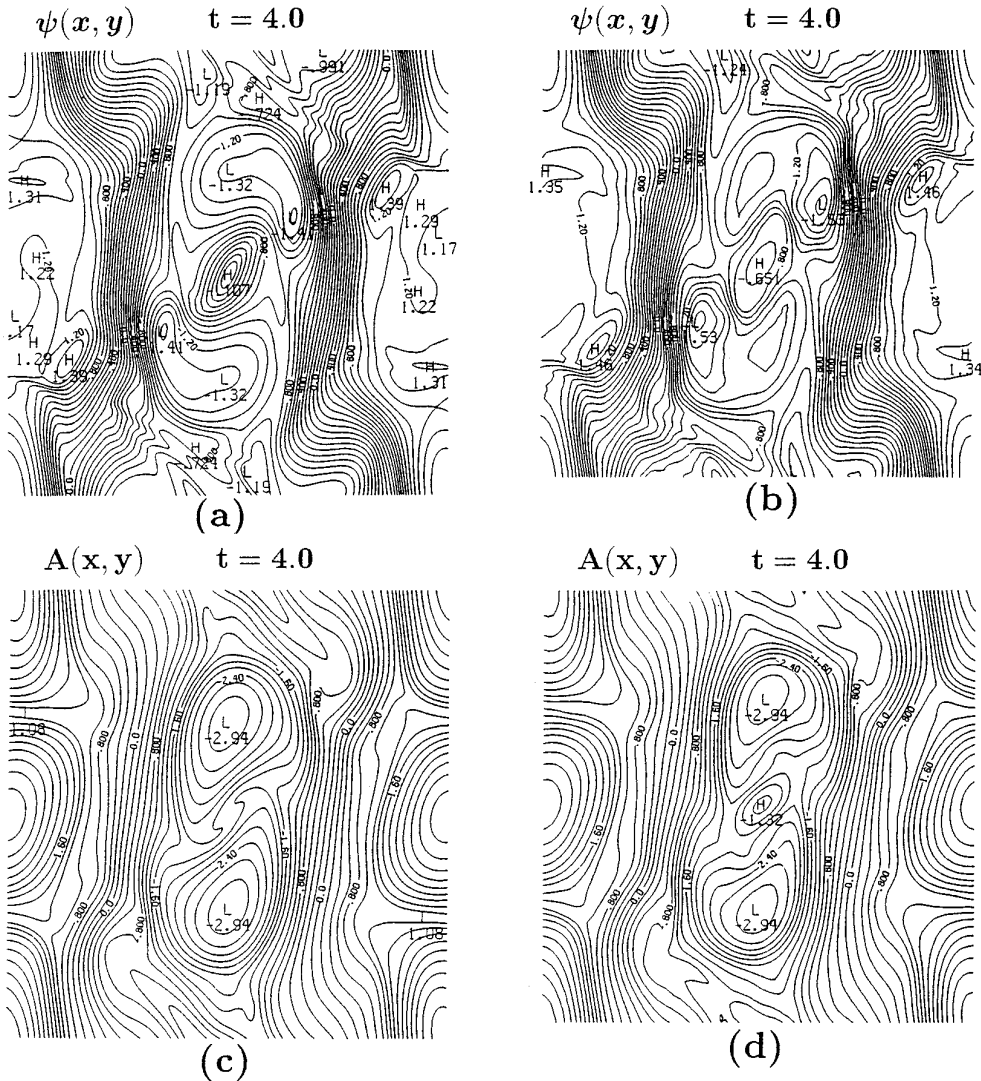
**FIG. 10.**   Contour lines of the stream function $\psi$ (a, b) and the magnetic potential $A$ (c, d) at $t = 4$ for the MHD runs M4 (a, c) and M6 (b, d); contour intervals are 0.1 for $\psi$ and twice that for $A$.

dissipation subrange, but keeps the speed advantage of the FFT to compute convolution products. The method has been tested in the one-dimensional case on the Burgers' equation, and in the two-dimensional case in MHD, for which resistive instabilities occur involving dissipative modes. Contrasted to hyperviscosity methods, such as those developed and tested in [4, 5] in 2D MHD as done here, the purpose and process whereby a simplified computation is performed are different; whereas here, the method is of a purely numerical nature, in the (linear or nonlinear) hyperviscous case, an attempt at simulating physical dissipative processes is made, with two drawbacks: in the linear case, oscillations develop, and in the nonlinear one, the cost is high in CPU (although it does remain lower than for a direct numerical simulation of equivalent effective

Taylor Reynolds number, as defined, for example, by the square of the computed ratio of integral to Taylor scales). More recently, it was also shown both analytically and numerically in the two-dimensional case that such methods develop spurious rings in vorticity and circulation [23].

The method, using a Fourier decomposition and a pseudo-spectral algorithm, is limited to homogeneous flows; this is to be contrasted, for example, to compact finite differences [24] which, because of their high precision, together with the possibility to easily implement them on parallel computers, are very versatile. Furthermore, the method proposed here is *not* an alternative to standard large-eddy simulations using a subgrid model which are of a more general character. Indeed, LES are not restricted to spectral computations, and their aim is the simulation of
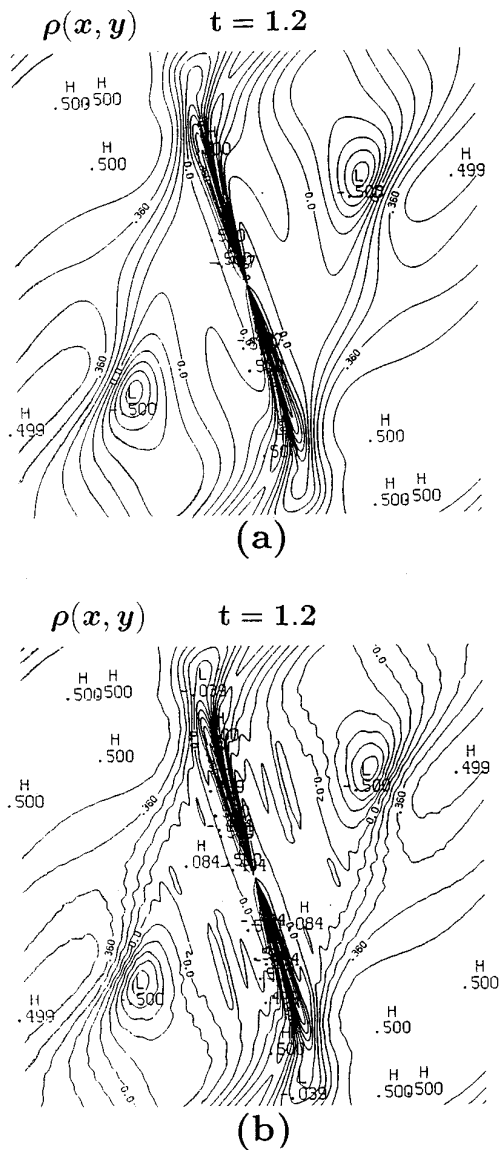
**FIG. 11.** Contour lines of the correlation coefficient between velocity and magnetic field $\rho(x, y)$ at $t = 1.2$ (normalised between $\pm 0.5$, see text) for the MHD runs M7 (a) and M6 (b). Only the window on the central current sheet is represented. Note the large spatial sectors within which $\rho(x, y)$ is close to its extrema, both in the large-scale structures and in the small-scale central current sheet.

of turbulent viscosity. In our calculations small scales are not necessarily isotropic, energy backscattering from small to large scales is present and, furthermore, phase correlations can exist between large and small wavenumbers. Dissipation retains its original linear character, leaving the nonlinear terms to produce in a self-consistent way the transport coefficients, and it is everywhere positive, as opposed to nonlinear hyperviscosity methods. As a consequence, coherent structures and intermittency are not suppressed at small scales, as was shown in the two examples given in this paper.
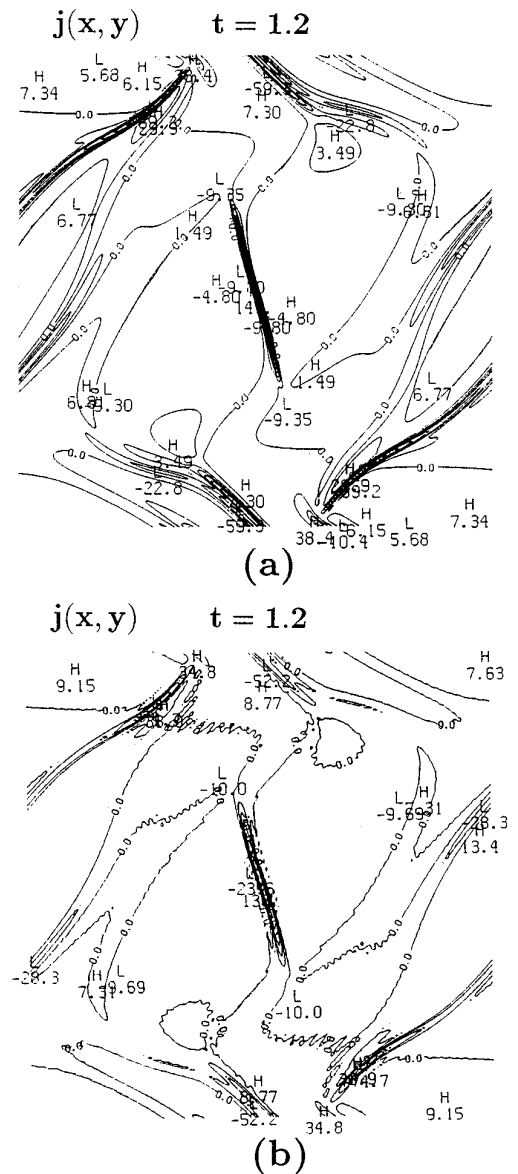


**FIG. 12.** Contour lines of the current density at $t = 1.2$ for the MHD runs M4 (a) and M6 (b). Maxima in the central current sheet are within 15% of each other, but the multigrid run is more noisy in the small scales.
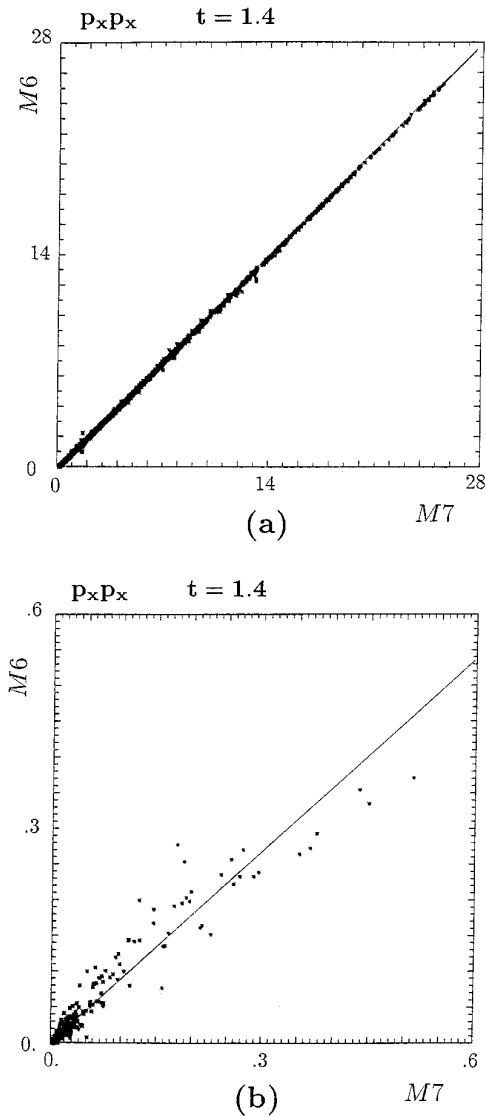
flows at much higher Reynolds numbers. Also, the subgrid scales can include a large fraction of the inertial subrange. We have not attempted to use our sparse-mode method in such a case. Our objective is more limited. We simply want to reduce the number of modes in the far dissipation range but leave enough of those modes to retain the essential physics. The type of simulation we are interested in could be coined as "almost a direct simulation," although this may be too optimistic. Indeed, we avoid most of the drawbacks of the large-eddy simulations using some form

**FIG. 13.** Scatter plot of the *xx*-component of the tensor $p_i p_j$, where $\mathbf{p} = \mathbf{v} + \mathbf{b}$. The test case (run M7) is in abscissa, and the sparse-model case (run M6) is on the ordinate; (a) the full data; (b) data in which large scales have been filtered out. The straight lines are best fit to the scatter plots.

An obvious application of the method is the simulation of three-dimensional turbulence, in order to study issues such as the small-scale structures of Euler and Navier–Stokes flows [25] and intermittency [26], and in particular the stability and dynamical interactions of vortex tubes.

## REFERENCES

1. P. Constantin, C. Foias, and R. Temam, *J. Fluid Mech.* **150,** 314 (1985).
2. A. Yoshizawa, *Phys. Fluids* **28,** 3313 (1985).
3. G. Erlebacher, M. Hussaini, C. Speziale, and T. Zang, *J. Fluid Mech.* **238,** 155 (1992).
4. T. Passot and A. Pouquet, *J. Comput. Phys.* **75,** 300 (1988).
5. T. Passot, H. Politano, A. Pouquet, and P. L. Sulem, *Theor. Comput. Fluid Dyn.* **1,** 47 (1990).
6. V. N. Denianski and E. A. Novikov, *Izv. Atmos. Oceanic Phys.* **10,** 127 (1974); *Prikl. Mat. Mech.* **38,** 507 (1974).
7. E. Vazquez-Semadeni and J. Scalo, *Phys. Rev. Lett.* **68,** 2921 (1992).
8. S. Grossman & D. Lohse, *Phys. Rev. Lett.* **67,** 445 (1991).
9. E. N. Lorenz, *Lecture Notes in Phys.,* Vol. 12 (Springer-Verlag, New York/Berlin, 1971), p. 195.
10. D. Gottlieb and S. A. Orszag, *Numerical Analysis of Spectral Methods Theory and Applications* (SIAM, Philadelphia, 1977).
11. G. Eyink, *Phys. D* **78,** 222 (1994).
12. P. S. Iroshnikov, *Sov. Astron.* **7,** 56 (1963).
13. R. H. Kraichnan, *Phys. Fluids* **8,** 995 (1965).
14. S. A. Orszag & C. M. Tang, *J. Fluid Mech.* **90,** 129 (1979).
15. H. Politano, A. Pouquet, and P. L. Sulem, *Phys. Fluids B* **1,** 2230 (1989).
16. H. Politano, A. Pouquet, and P. L. Sulem, *Cargèse Workshop on MHD flows, July 1988,* edited by M. Meneguzzi, A. Pouquet, and P. L. Sulem (North-Holland, Amsterdam, 1989).
17. H. Politano, P. L. Sulem, and A. Pouquet, *Topological Fluid Mechanics,* edited by H. K. Moffatt and A. Tsinober (Cambridge Univ. Press Cambridge, 1990).
18. D. Biskamp, H. Welter, and M. Walter, *Phys. Fluids B* **2,** 3024 (1990).
19. W. H. Matthaeus and D. Montgomery, *Ann. N.Y. Acad Sci.* **357,** 203 (1980).
20. G. Einaudi, C. Chiuderi, and F. Califano, *Adv. Space Res.* **13,** 85 (1993).
21. A. Pouquet, in *Magnetohydrodynamic Turbulence,* Les Houches Session XLVII, edited by J. P. Zahn and J. Zinn-Justin (Elsevier, Amsterdam, 1993), p. 139.
22. R. Grappin, *Phys. Fluids* **29,** 2433 (1986).
23. X. Jimenez, *J. Fluid Mech.* **279,** 169 (1994).
24. S. Lele, *J. Comput. Phys.* **103,** 16 (1992).
25. A. Vincent and M. Meneguzzi, *J. Fluid Mech.* **225,** 1 (1991).
26. Z. S. She, S. Chen, G. Doolen, R. H. Kraichnan, and S. A. Orszag, *Phys. Rev. Lett.* **70,** 3521 (1993).